Journal of Magnetic Resonance 204 (2010) 200–207

Contents lists available at ScienceDirect

Journal of Magnetic Resonance

journal homepage: www.elsevier.com/locate/jmr

High fidelity magnetic resonance imaging by frequency sweep encoding and Fourier decoding

Jun Shen *, Yun Xiang

Molecular Imaging Branch, National Institute of Mental Health Intramural Research Program, NIH, Bethedsa, MD, USA

ARTICLE INFO

Article history:
Received 2 December 2009
Revised 16 February 2010
Available online 20 February 2010

Keywords:
Magnetic resonance imaging
Encoding
Decoding
Field distortion

ABSTRACT

Using a RF pulse with linear frequency sweep and a simultaneous encoding gradient, magnetization is sequentially excited accompanied by a quadratic phase profile. This quadratic dependence of magnetization phase on position dephases magnetization away from its vertices, allowing direct spatial encoding and image formation in the time domain. In this work, we show that Fourier decoding or least square fitting in combination with frequency sweep spatial encoding schemes can generate high fidelity images and we also extend spatial encoding to include nonlinear frequency sweep. Application to in vivo multi-scan susceptibility-weighted imaging is demonstrated. Our results show that Fourier-decoded, spatially encoded images compare favorably with conventional high resolution images while preserving the unique features of sequential excitation.

Published by Elsevier Inc.

1. Introduction

The dominating schemes for magnetic resonance imaging have been based on the Fourier transform relationship between *k* space and image space [1,2]. To generate conventional multidimensional images, *k* space is sampled by the use of incremental phase encoding in the absence of RF pulses. In its ultimate form, a two-dimensional *k* space can be sampled in a single scan as in echo-planar imaging (EPI) [3]. Because of the fundamental role of phase encoding in magnetic resonance imaging, a great deal of effort has been made to exploring alternative multi- and single-scan phase and/or spatial encoding methods (e.g., [4–9]). Notably, BURST-type imaging methods using phase encoding generated by various DANTE pulses [10] have been developed [5]. This fundamentally different phase-encoding concept is based on the realization that each band excited by a DANTE pulse train in the presence of a constant gradient is phase-encoded with accumulated phase proportional to the frequency offset of the band. As such, the DANTE bands can be read out sequentially in the *k* space by a constant readout gradient with each band forming a separate echo, thus allowing single scan imaging without EPI-type switching gradients [5].

The BURST-type imaging methods suffer from low sensitivity because conventional DANTE pulses can only excite a fraction of available equilibrium magnetization. To improve sensitivity, Cho and Ro [6] proposed multi- and single-scan phase encoding imaging using frequency-modulated DANTE pulses. The frequency sweeping nature of the frequency-modulated DANTE pulses minimizes RF interference among neighboring bands, allowing excitation and encoding of close to 100% of the available magnetization. In comparison to EPI-type imaging methods, phase encoding based on frequency-modulated DANTE pulses still suffers sizable loss in sensitivity because each pixel has a quadratic phase profile with the vortex of the phase parabola centered at the pixel center, leading to intravoxel dephasing.

In contrast to methods based on frequency-modulated DANTE pulses Pipe [11] used a continuous chirp pulse for linear frequency sweep excitation and encoding and subsequent readout along the frequency sweep dimension. The quadratic dependence of magnetization phase on position due to sequential excitation by the chirp pulse allows dephasing of magnetization away from the vertex and direct image formation in the time domain. Since only the vertices of the phase parabolas are sampled, penalty in sensitivity associated with the frequency-modulated DANTE method [6] is eliminated. The usefulness of spatial encoding by linear frequency sweep excitation was demonstrated in vivo for generating multi-scan sparse images (time-of-flight magnetic resonance angiography, Ref. [11]). Pipe further showed resolution of spatially encoded images can be improved using a quadratic reconstruction procedure [11].

Recently, Frydman et al. [12] proposed an ingenious technique for single scan two-dimensional spectroscopy. In this technique, the magnetization is sequentially excited to allow parallel t_1-evolution across the sample. During subsequent readout using a gradient pulse (or a train of EPI-type gradient pulses) a spectrum is directly formed in the time domain corresponding to the F_1-projection of a

* Corresponding author. Address: Molecular Imaging Branch, National Institute of Mental Health, Bldg. 10, Rm. 2D51A, 9000 Rockville Pike, Bethesda, MD 20892-1527, USA. Fax: +1 301 480 2397.
E-mail address: shenj@intra.nimh.nih.gov (J. Shen).

1090-7807/$ - see front matter Published by Elsevier Inc.
doi:10.1016/j.jmr.2010.02.014

conventional two-dimensional NMR spectrum. Extending this scheme to single scan two-dimensional MRI, Frydman et al. [13,14] proposed several novel mechanisms for directly forming spatial images in the time domain using linear frequency sweep encoding. In combination with EPI-type readout, the Frydman et al.'s new single scan imaging methods has found applications in spin–echo imaging of both human and rat brains [15,16]. The unique sequential excitation of magnetization inherent in frequency sweep encoding promises to open an interesting venue for novel image contrast generation and for designing new imaging methods such as in magnetic resonance angiography [11]. Sequential excitation of magnetization has proven to be highly valuable in minimizing geometrical distortions in single scan imaging under severe B_0 field inhomogeneity [15–17].

In this work, we extend current spatial encoding by linear frequency sweep to include nonlinear frequency sweep schemes and show that Fourier decoding or least square fitting in combination with frequency sweep spatial encoding can generate high fidelity anatomical images. Application to in vivo multiscan susceptibility-weighted imaging at 11.7 T is demonstrated. Our results show that Fourier-decoded, spatially encoded images compare favorably with conventional high resolution images while preserving the unique features of sequential excitation. A preliminary account of this work has been submitted as a meeting abstract to the 18th annual meeting of the International Society of Magnetic Resonance in Medicine.

2. Theory

The theoretical framework developed by Frydman et al. [13,14] and notations therein were used here to explain the mechanisms of spatial encoding using linear frequency sweep. Using a RF pulse with linear frequency sweep such as a chirp pulse and a simultaneous encoding x gradient, magnetization is sequentially excited along the direction of the applied encoding gradient [12]. The phase of the magnetization at the end of sequential excitation has a quadratic dependence on the x position of the magnetization as explained by Frydman et al. [12,13]:

$$\phi^{\text{encoding}}(x) = ax^2 + bx + c \tag{1}$$

where the constants a, b and c depend on frequency sweep and encoding gradient parameters [12,13]. Upon reversing the polarity of the encoding gradient a gradient echo is formed in the time domain with the following phase relationship:

$$\phi^{\text{readout}}(k(t), x) = \phi^{\text{encoding}} - 2\pi k(t)x \tag{2}$$

where $k(t)$ represent k values as a linear function of time. Using Frydman et al.'s argument [12,13], signals at a certain $k(t)$ point arise mostly from spin packets at x_k with x_k determined by

$$\{d\phi^{\text{readout}}(k(t), x)/dx\}_{x=xk} = 0 \tag{3}$$

At $x \neq x_k$, signals are largely dephased by the internal quadratic phase profile around x_k. As a result, an image can be directly formed in the time domain according to Eq. (15) in Ref. [13]:

$$F(k(t)) \approx \rho(x_k)\exp(i\phi^{\text{encoding}}(x_k)) \times \int_{x\approx xk} \exp[i(d^2\phi^{\text{encoding}}(x)/dx^2)_{x=xk}(x-x_k)^2/2]dx \tag{4}$$

We note that, numerically, the spatially encoded time domain image $F(k(t))$ can also be expressed in matrix form for one-dimensional encoding using an arbitrary frequency sweep scheme:

$$\mathbf{F} = \mathbf{EP} \tag{5}$$

where matrix $\mathbf{E}$ ($M \times N$) represents the linear relationship between the time domain image vector $\mathbf{F}$ ($M \times 1$) and the relaxation-weighted spin density vector $\mathbf{P}$ ($N \times 1$) with $M \geqslant N$. Element mn of matrix $\mathbf{E}$ is given by a phasor

$$E_{mn} = \exp(i(\phi^{\text{readout}}(k(m\Delta t), n\Delta x)) \tag{6}$$

where Δt and Δx denote sampling intervals in the k space and image (x) space, respectively. Eq. (5) can be solved numerically using the least square fitting procedure for $M \geqslant N$:

$$\mathbf{P} = (\mathbf{E}^{\dagger}\mathbf{E})^{-1}\mathbf{E}^{\dagger}\mathbf{F} \tag{7}$$

where '†' denotes conjugate transpose. Alternatively, the phase terms in $\mathbf{E}$ can be factored out because each row in matrix $\mathbf{E}$ has the same position-dependent high order phase profile:

$$\mathbf{F} = \hat{\mathbf{E}}\mathbf{\Phi}\mathbf{P} \tag{8}$$

where $\mathbf{\Phi}$ is a $N \times N$ diagonal matrix with elements given by

$$\mathbf{\Phi}_{nn} = \exp(i\pi f(n/N - 0.5)\text{SW} \times T_p) \tag{9}$$

and $\hat{\mathbf{E}}$ is proportional to the unitary Fourier matrix for $M = N$ because it contains linear and constant phase terms only. SW and T_p denote the frequency sweep width and duration of the chirp pulse, respectively. $f(x)$ denotes the high order phase profile resulted from frequency sweep excitation. For linear frequency sweep, $f(x) = x^2$. Sequentially multiplying Eq. (8) by $\hat{\mathbf{E}}^{\dagger}$ and $\mathbf{\Phi}^{\dagger}$, one obtains:

$$\mathbf{P} = \mathbf{\Phi}^{\dagger}\hat{\mathbf{E}}^{\dagger}\mathbf{F} \tag{10}$$

Eq. (11) allows direct inverse Fourier transform of the spatially encoded time domain image vector $\mathbf{F}$ ($M \times 1$) to generate an image vector $\mathbf{P}$ in the conventional image space of the same size with or without correcting for $\mathbf{\Phi}^{\dagger}$. That is

$$|\mathbf{P}| = |\hat{\mathbf{E}}^{\dagger}\mathbf{F}| \tag{11}$$

3. Methods

Male Sprague–Dawley rats (~200 g body weight, Taconic, Germantown, NY, USA) were orally intubated and mechanically ventilated with a mixture of ~70% N_2O, 30% O_2 and 1.5% isoflurane. The ventilation rate was synchronized with imaging TR to minimize motion artifacts. The left femoral artery was cannulated for periodically sampling arterial blood to monitor blood gases (pO_2, pCO_2), pH and glucose concentration using a blood analyzer (Bayer Rapidlab 860, East Walpole, MA, USA), and for monitoring arterial blood pressure levels. Rectal temperature was monitored and maintained using an external pump for heat exchange by water circulation (BayVoltex, Modesto, CA, USA). Heart rate, end-tidal CO_2 and tidal pressure of ventilation were monitored continuously. Normal physiology conditions were maintained during the course of imaging acquisition. All procedures were approved by the National Institute of Mental Health Animal Care and Use Committee.

NMR experiments were performed on a Bruker spectrometer (Bruker Biospin, Billerica, MA, USA) interfaced to an 11.7 T (500.14 MHz) 89-mm bore vertical magnet (Magnex Scientific, Abingdon, UK) and a 56-mm i.d. water-cooled Mini0.5 gradient insert (rise time = 100 μs, maximum gradient strength = 30 G/cm, Bruker Biospin, Billerica, MA, USA). A home-built single-turn 1-cm i.d. surface RF transmit/receive coil integrated to an animal handling system [18] was used. The rat brain was shimmed as previously described using the FLATNESS (five linear acquisitions for up to third order noniterative, efficient slice shimming) method [19] to correct the 1st–3rd order in-slice and through slice B_0 inhomogeneity. The two-dimensional version of the gradient echo imaging sequence was schematically depicted in Fig. 1 and programmed using Paravision 3.0.1 (Bruker Biospin, Billerica, MA, USA). A T_p = 8 or 16 ms modified chirp pulse of θ° (nominal 90° corresponding to γB_1 = 750 or 375 Hz, 2048 points) was used for

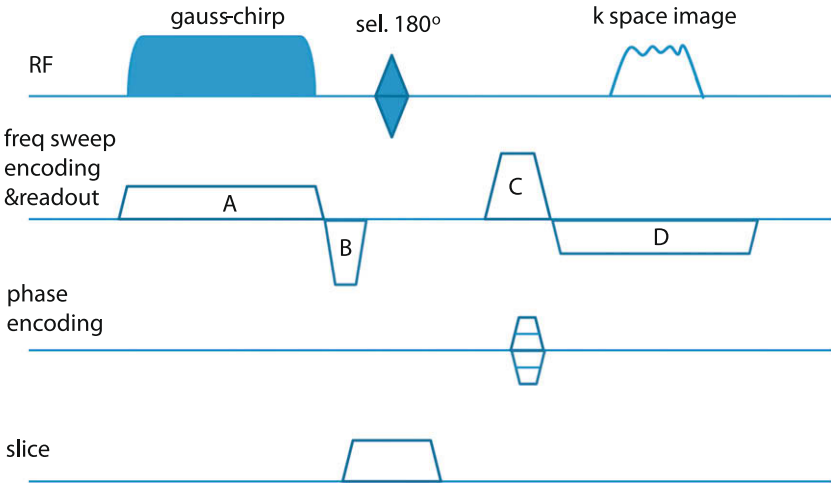

Fig. 1. Schematic drawing of the two-dimensional version of the proposed gradient echo imaging sequence using frequency sweep spatial encoding. A modified chirp pulse (gauss-chirp) of $\theta°$ was used for frequency sweep spatial encoding. The encoding and readout gradients were applied along the x direction. A slice was selected using either a 180° amplitude-modulated pulse or two identical 180° adiabatic full passage pulses. For three-dimensional imaging, the 180° slice selective pulse(s) and slice gradient can be replaced by phase encoding along the third spatial dimension. After frequency sweep spatial encoding, the x gradient was essentially reversed twice. To shorten the minimum TE, the first reversal of the x gradient was interrupted by the slice-selective 180° pulse(s). The gradients areas satisfy A = B + C = D. The k-space data were sampled during the second gradient reversal (D). As a result, a FIFO (First In, First Out) readout was accomplished with equal TE (T_2^*) for the spins excited sequentially by the modified chirp pulse. Conventional multistep phase encoding was employed in the y direction. Crusher gradients and reversal of the conventional phase encoding gradients were not drawn for clarity.

frequency sweep encoding. Both edges of the original chirp pulse were rounded off by a half-Gaussian pulse truncated at 1% with a pulse duration of $T_p/8$. The modified chirp pulse has a frequency sweep width (SW) of 64 kHz and a linear sweep rate of 8 MHz/s for T_p = 8 ms or SW = 32 kHz for T_p = 16 ms. The modified chirp pulse and its characteristics are shown in Fig. 2. The frequency sweep encoding and readout gradients (3200 Hz/mm for T_p = 8 ms, which is 25% of maximum gradient strength; 1600 Hz/mm for T_p = 16 ms) were applied to the x direction. For two-dimensional gradient echo imaging a 1 or 2 mm coronal (z) slice was selected using either one 2-ms 180° MAO pulse [20] or two identical 180° adiabatic hyperbolic secant pulses ([21], 2 ms each, μ = 4, 1% truncation). For three-dimensional imaging, the 180° slice selective pulse(s) and slice gradient can be replaced by phase encoding along the third spatial dimension. To minimize geometrical distortion, the spatially encoded image was read out to generate equal TE for the sequentially excited magnetization [11,15,16]. That is, spins excited sequentially by the modified chirp pulse were read using a FIFO (First In, First Out) method. This was achieved here in the gradient echo imaging experiment by sampling the k-space data during the second gradient reversal. Conventional multistep phase encoding was used in the y direction. FOV = 20 mm × 20 mm. Matrix size = 512 × 512. TR ≈ 1 s. For T_p = 8 ms, spectral width = 64 kHz, acquisition time = 8 ms, T_2^* delay time (for generating

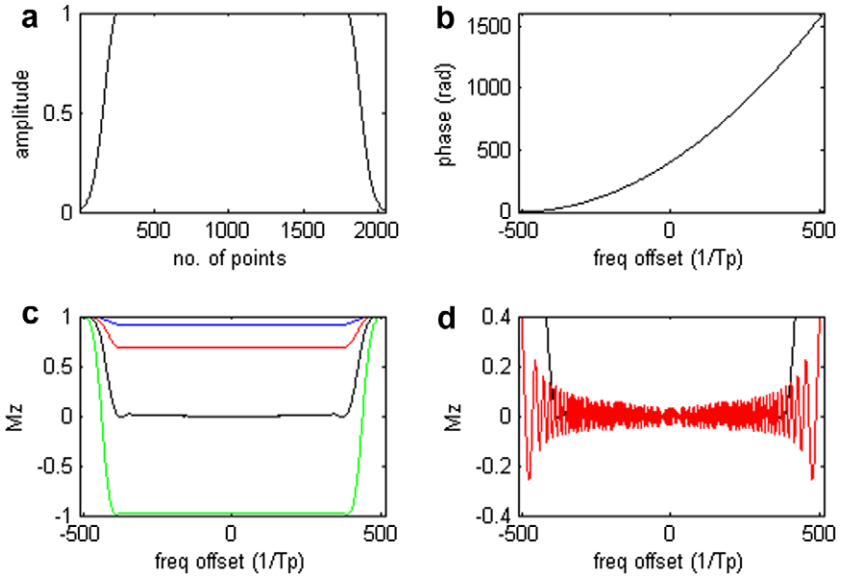

Fig. 2. (a) Normalized amplitude profile of the modified chirp pulse. The rectangular edges ($0 \sim 1/(8{*}T_p)$ and $7{*}T_p/8 \sim T_p$) of the original chirp pulse were replaced by half-Gaussian pulses with truncation at 1% level with no modifications of the linear frequency sweep. (b) Magnetization phase profile excited by the modified chirp pulse. (c) M_z magnetization after execution of the modified chirp pulse at γB_{1max} = 0.25× (blue), 0.5× (red), 1.0× (black) and 2.5× γB_{1max}90° (green). (d) Comparison of residual M_z excited by original chirp pulse (red) and the modified chirp pulse with Gaussian edges (black). θ = 90°. The frequency scale in (b–d) is normalized to $1/T_p$.

susceptibility contrast) = 10 ms (8 ms sequential excitation, 8 ms sequential readout and 2 ms additional T_2^* delay); For T_p = 16 ms, spectral width = 32 kHz, acquisition time = 16 ms, T_2^* delay time = 16 ms (16 ms sequential excitation, 16 ms sequential readout).

For Fourier reconstruction along both frequency sweep (x) and conventional phase (y) encoding directions, the k-space data were directly Fourier transformed based on the analysis given in Theory (Eqs. (5)–(11)). Identical magnitude images were obtained with or without correcting high order phase (Eq. (11)). In order to generate susceptibility-weighted real, imaginary and phase images the quadratic term of the frequency sweep phase profile calculated from Eq. (10) was used to correct the 2nd order phase of the Fourier transformed image along the frequency sweep encoding direction. This was possible because the quadratic phase term of the modified chirp pulse equals in magnitude to that of the magnetization at the end of the excitation [14]. After the 2nd order phase correction, the image data were inversely Fourier transformed in both dimensions. The central portion (32×32) of the regenerated k-space data was extracted and apodized using a two-dimensional Hanning filter and then Fourier transformed to produce a low-pass filtered 512×512 image. Finally, the original 2nd order phase corrected image was demodulated using the phase of the low-pass filtered image [22]. For direct spatially encoded time domain image formation along the x direction two-dimensional images were formed using one-dimensional Fourier transform along the conventional phase encoding direction only. For numerical simulations, computer programs were developed in-house using MATLAB (The MathWorks, Inc., Natick, MA, USA) for solving Bloch equations without relaxation terms and for postacquisition imaging processing based on Eqs. (7), (10) and (11).

4. Results

4.1. Pulse shaping

Fig. 2(a) shows the amplitude profile of the modified chirp pulse. The rectangular edges ($0 \sim (1/8)T_p$) and ($(7/8)T_p \sim T_p$) of the original chirp pulse were rounded off by half-Gaussian pulses with truncation at 1% level ($\exp[-(4\log 100(0.125t/T_p - 0.5)^2]$ with no modifications of the linear frequency sweep (frequency sweep rate = 8 MHz/s for T_p = 8 ms). The flip angle independent phase profile of the excited magnetization was also shown which has a characteristic parabolic shape with its curvature described by Eqs. (1) and (9), essential for frequency sweep encoding (see Fig. 2(b)). Fig. 2(c) compares residual longitudinal magnetization after execution of the modified chirp pulse at $\gamma B_{1max} = 0.25\times$, $0.5\times$, $1.0\times$ and $2.5\times$ $\gamma B_{1max}90°$, demonstrating the insensitivity of the shape of its frequency responses with respect to flip angles. $\gamma B_{1max}90°$ represents the peak RF amplitudes for $\theta = 90°$. Fig. 2(d) compares residual M_z excited by the original chirp pulse at $\theta = 90°$ with that by the modified chirp pulse with Gaussian edges. As shown by Fig. 2(c) and (d), replacing the abrupt edges of the original chirp pulse leads to a well-behaved band-selective frequency sweep pulse with an approximately top-hat frequency response and a bandwidth highly insensitive to flip angles. Like the original chirp pulse, this pulse also behaves adiabatically once $\theta = 180°$ is reached (see Fig. 7 in Ref. [13]). Noticeably, the undesirable oscillation of magnetization associated with the original rectangular chirp pulse is eliminated. Based on numerical simulation of Bloch equations, the bandwidths of the modified chirp pulse at half maximum of 90° excitation (BWHM90°) and 180° inversion (BWHM180°) were found to be BWHM90° $\times T_p$ = 412 and BWHM180° $\times T_p$ = 436, respectively; the peak RF amplitudes for $\theta = 90°$ ($\gamma B_{1max}90°$) and for $\theta = 180°$ ($\gamma B_{1max}180°$) were found to be $\gamma B_{1max}90° \times T_p = 6.0$ and $\gamma B_{1max}180° \times T_p \geqslant 15.0$, respectively.

4.2. Image reconstruction

The image formation in time domain based on internal dephasing of signals from $x \neq x_k$ in Eq. (4) is simulated numerically by integrating signal contribution from the entire sample to the spatially encoded image $F(k(t))$. Fig. 3(a) compares a one-dimensional sample with a half sine-shaped ($\sin(x)$, $x \sim [0, \pi]$) spin density distribution. The sample was positioned at the center of field of view (20 mm, represented by $2 \times -16 \times 1024$ discrete points). Parameters for gradient, the modified chirp pulse and data acquisition used in simulation were identical to those employed in in vivo experiments with T_p = 8 ms as described in Section 3 except that, since relaxation was ignored in numerical simulation, k space image was read out LIFO (Last In, First Out) during the first gradient reversal. The simulated spatially encoded image closely matches $\rho(x)$ except at the edges of the half-sine function where $\rho(x) \approx 0$. The corresponding images formed in the x space by Fourier transform (Eq. (11)) and least square fitting (Eq. (7)) were also shown. No significant deviations of the x-space images from $\rho(x)$ were found using either Fourier transform or least square fitting. Relatively large deviations of the spatially encoded image from $\rho(x)$ are seen when the half sine-shaped $\rho(x)$ is replace by a rectangle function ($\Pi(x)$). In contrast, both Fourier transformed and least square fitting as outlined in Theory are able to generate high fidelity images.

Fig. 4 compares in vivo coronal rat brain images formed using different mechanisms. The conventional gradient echo image is shown in Fig. 4(a). This image was acquired by replacing the modified chirp pulse and the frequency sweep encoding gradient in Fig. 1 with a nonselective rectangular hard pulse. Slicethickness = 1 mm. FOV = 20 mm × 20 mm. Matrix size = 512×512. TR ≈ 1 s. TE = 16 ms (from the center of the rectangular pulse to the center of the gradient echo). No. of averages = 1. Fig. 4(b) and (c) shows images acquired using frequency sweep encoding with T_p = 16 ms. Slicethickness = 1 mm. FOV = 20 mm × 20 mm. Matrix size = 512×512. TR ≈ 1 s. Spectral width = 32 kHz. Acquisition time = 16 ms, T_2^* delay time = 16 ms. No. of averages = 1. In Fig. 4(b), Fourier transform was performed along the conventional phase encoding direction (anterior–posterior) only. The hybrid image shows fewer anatomical details seen in the conventional gradient echo image. For example, the neocortical veins and venules perpendicular to B_0, which show high contrast in Fig. 4(a), are difficult to discern along the frequency sweep direction (left–right) in the hybrid image. The midline fissure, which has an effect on the time domain spatially encoded image similar to the edges of the $\Pi(x)$ function (see Fig. 3(b)) is largely obscured by incomplete internal 2nd order dephasing. Similarly, significant geometrical deformation and intensity oscillation on both sides of the skull are also seen in the hybrid image. Upon Fourier transform along the frequency sweep direction, a high fidelity image, comparable to the high resolution conventional anatomical image (Fig. 4(a)), was obtained as shown in Fig. 4(c), despite the use of relatively long echo time. In addition, the geometrical distortions seen in the hybrid image were completely eliminated after Fourier transform. Notice that the signal void in the extracranial tissue at the left and right edges in Fig. 4(c) is mainly due to the frequency profile of the modified chirp pulse. There was no excitation of magnetization at the left and right edges of the field of view (see Fig. 2(c)).

The usefulness of the Fourier decoding with frequency sweep encoding for high resolution multiscan imaging of microsusceptibility is demonstrated in Fig. 5. A coronal gradient echo image with high SNR was acquired using frequency sweep encoding along the left–right direction. T_p = 8 ms. Slicethickness = 2 mm. FOV = 20 mm × 20 mm. Matrix size = 512×512. TR ≈ 1 s. Spectral width = 64 kHz. Acquisition time = 8 ms, T_2^* delay time = 10 ms (8 ms sequential excitation, 8 ms sequential readout and 2 ms

additional T_2^* delay). No. of averages = 4 (for enhanced SNR and contrast-to-noise ratio). Fig. 5(a) shows the T_2^*-weighted hybrid magnitude image after Fourier transform along the conventional phase encoding direction (anterior–posterior) only. Figs. 5(b)–(e) show the magnitude (b), real (c), imaginary (d) and phase (e) images after Fourier transform along both the frequency sweep encoded direction (left–right) and the conventional phase encoding direction (anterior–posterior) followed by correction of 2nd order phase (Eq. (10)) and homodyne demodulation [21] as described in Section 3. Clearly, high fidelity images were obtained with Fourier decoding accompanied by a larger coverage along the spatially encoded direction. High susceptibility contrasts (e.g., gray matter vs. white matter, venules vs. brain tissue) can be clearly seen in the Fourier-decoded images, especially in the imaginary (Fig. 5(d)) and phase (Fig. 5(e)) images. (The intrinsic contrast-to-noise ratios in the imaginary and phase images are much higher than the magnitude and real images. The advantages of phase imaging at high magnetic field have recently been analyzed and demonstrated [23].)

To further illustrate the usefulness of Fourier decoding and least square fitting, Fig. 6 shows numerical simulation results for a nonlinear frequency sweep scheme. The rate of the nonlinear frequency sweep is $\alpha(1-\beta(t/T_p)^2)$. α and β are related by $\alpha(1-\beta/12) = SW/T_p$. The amplitude modulation of this nonlinear frequency sweep pulse is identical to that used in Fig. 3 while its phase contains both quadratic (t^2) and quartic (t^4) terms. Using this new frequency sweep scheme we repeated the numerical simulation shown in Fig. 3 for $\beta = 1$ with all other parameters unchanged. Compared to Fig. 3, inclusion of the quartic phase term ($\beta = 1$) actually narrows the spatially encoded time domain image (see Fig. 6). Regardless of the difference in phase profiles between Figs. 3 and 6, both Fourier and least square fitting are capable of producing high fidelity images.

5. Discussion

Rounding off of the rectangular edges of the original chirp pulse was found to produce a well-behaved frequency sweep pulse with a close to "top hat" profile. This "top hat" profile is maintained regardless of the actual flip angle of excitation or inversion. This behavior has allowed us to use a surface transmit/receive coil with high B_1 inhomogeneity for our experiments. It also makes it possible to use spatial encoding for small flip angle imaging experiments in a fashion similar to FLASH two-dimensional or three-dimensional imaging [24]. The low flip angle also eases SAR concerns. We note that three-dimensional spin–echo imaging using frequency sweep encoding along the slice direction has been applied to human studies under the SAR constraint [15].

Previously, Pipe proposed a quadratic reconstruction method ([11]) analogous to discrete Fourier transform for improving resolution of spatially encoded images. Using the quadratic reconstruction method each position is reconstructed after applying a position-dependent quadratic phase correction to each time point in the echo along the linear frequency sweep direction. In this work, we show that the spatially encoded images can be reconstructed by directly applying fast Fourier transform to the echo ($|\mathbf{P}| = |\hat{\mathbf{E}}^{\dagger}\mathbf{F}|$ in Section 2). Quadratic phase correction for linear frequency sweep is necessary only when phase-sensitive images are needed. Furthermore, we demonstrate that Fourier decoding can be applied to arbitrary (nonlinear) frequency sweep schemes. However, it should be noted that Fourier decoding nonetheless introduces constraints and artifacts associated with discrete Fourier transform such as Gibbs ringing (shown in Figs. 3 and 6) and aliasing when the minimum Nyquist sampling rate is violated. We note that Fourier aliasing may become advantageous in parallel imaging using multiple receive coils to acquire spatially encoded images.

The difference in the apparent fidelity of spatially encoded time domain images shown in Figs. 3 and 6 warrants further comments. In conventional Fourier imaging, the point spread function (PSF) is approximately described by $\sin c(x/\Delta x - n)/\mathrm{sinc}(x/\mathrm{FOV})$. (The effect of truncating the k space echo by the finite sampling window gives rise to the slow varying denominator.). However, the concept of a spin density distribution-independent point spread function as currently defined as a convolution factor is not applicable to spatially encoded time domain images (That is, $F(k(t)) \neq \rho(x_k) \otimes \mathrm{PSF}$). This point is illustrated by the results given in Fig. 3. For the $\sin(x)$ ($x \sim [0, \pi]$) spin density distribution (Fig. 3(a)) the close match between $F(k(t))$ and $\rho(x_k)$ would have suggested that $\mathrm{PSF} \approx \delta(x_k)$ if $F(k(t)) = \rho(x_k) \otimes \mathrm{PSF}$ were applicable to spatially encoded time domain images. The same $\mathrm{PSF} \approx \delta(x_k)$ cannot describe the significantly larger discrepancy between $F(k(t))$ and $\rho(x_k)$ for the rectangle spin density distribution ($\Pi(x)$) shown in Fig. 3(b). While the point spread function of the conventional Fourier images ($\approx \sin c(x/\Delta x - n)$) can be seen as a result of the orthogonality of the Fourier matrix Fig. 3(b) demonstrates that the internal dephasing in k space images based on the positional quadratic phase profile (Eq. (4)) limits spatial resolution. This limitation on spatially

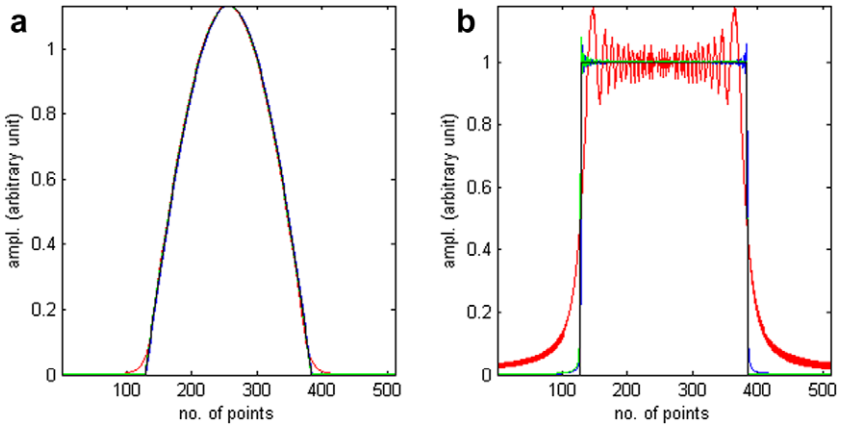

Fig. 3. (a) Spatially encoded time domain image (red), its Fourier transform (blue) and least square fitted image (green) of a one-dimensional sample with a half sine-shaped ($\sin(x)$, $x \sim [0, \pi]$) spin density distribution (black). (b) Spatially encoded time domain image (red), its Fourier transform (blue) and least square fitted image (green) of a one-dimensional sample with a rectangle function ($\Pi(x)$) spin density distribution (black). The samples were positioned at the center of field of view (20 mm, represented by $2 \times -16 \times 1024$ discrete points). Parameters for gradients, the modified chirp pulse and data acquisition used in simulation were identical to those employed in in vivo experiments with $T_p = 8$ ms as described in Section 3 except that k space images were formed during the first gradient reversal (First In, Last Out). Note that the numerically simulated conventional magnitude images are identical to the corresponding spatially encoded Fourier-decoded images (blue).

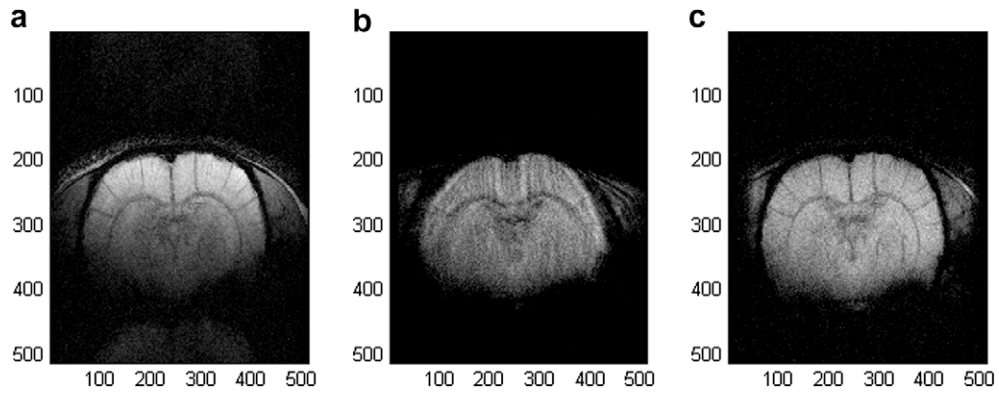

Fig. 4. (a) Conventional gradient echo magnitude image. Slicethickness = 1 mm. FOV = 20 mm × 20 mm. Matrix size = 512 × 512. TR ≈ 1 s. TE = 16 ms (from the center of the rectangular pulse to the center of the gradient echo). No. of averages = 1. (b) Hybrid magnitude image with no Fourier transform along the frequency sweep encoding direction. T_p = 16 ms. Slicethickness = 1 mm. FOV = 20 mm × 20 mm. Matrix size = 512 × 512. TR ≈ 1 s. Spectral width = 32 kHz. Acquisition time = 16 ms, T_2^* delay time = 16 ms. No. of averages = 1. (c) Magnitude image obtained after Fourier transform of (b) along the frequency sweep direction.

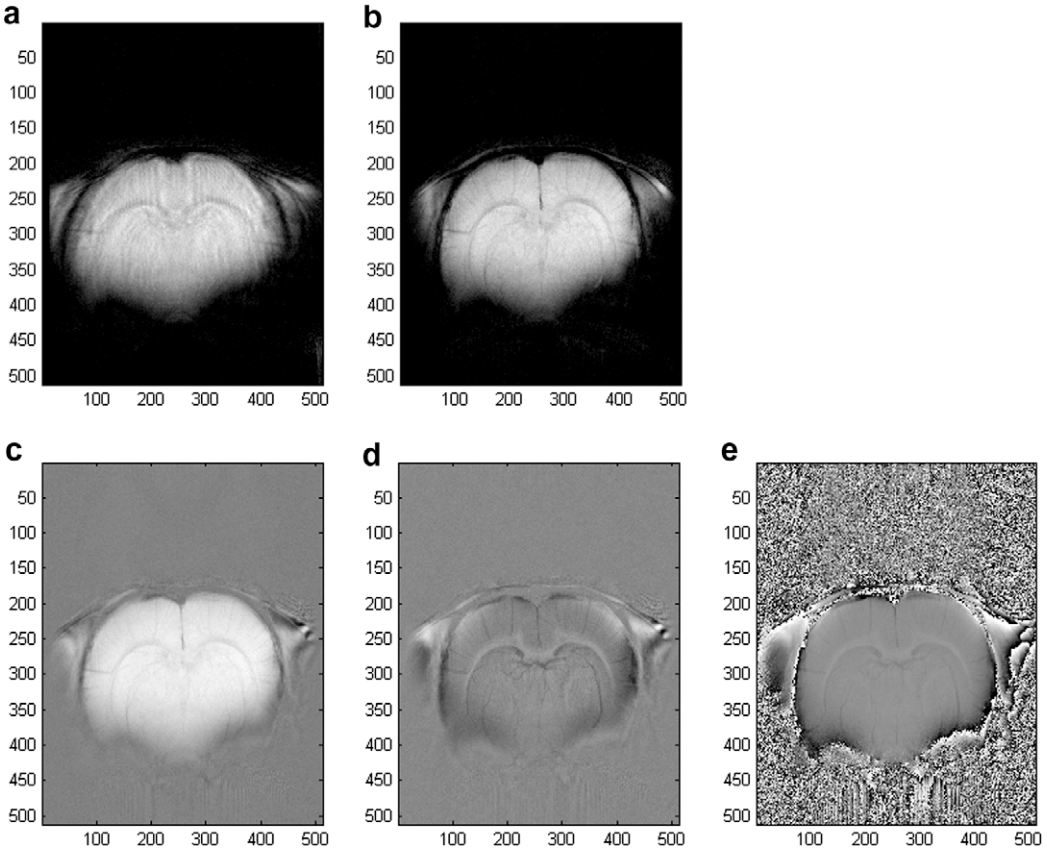

Fig. 5. (a) A coronal hybrid magnitude image of rat brain using frequency sweep encoding along the left–right direction. No Fourier transform along the frequency sweep direction was applied. T_p = 8 ms. Slicethickness = 2 mm. FOV = 20 mm × 20 mm. Matrix size = 512 × 512. TR ≈ 1 s. Spectral width = 64 kHz. Acquisition time = 8 ms, T_2^* delay time = 10 ms. No. of averages = 4. (b–e) Fourier-decoded magnitude (b), real (c), imaginary (d) and phase (e) images with 2nd order phase correction and homodyne demodulation.

encoded images puts high demand on hardware and SAR. As illustrated by Figs. 3–6 Fourier decoding can overcome these limitations and produce images compare favorably with conventional high resolution images while preserving the unique features of sequential excitation.

The least square fitting procedure given by Eq. (7) as well as the Fourier decoding method given by Eqs. (10) and (11) are generally applicable to image reconstruction from any *k*-space data (e.g., one may generate *k* space echoes using nonlinear frequency sweeps or an arbitrary frequency sweep with an arbitrary amplitude modulation, etc. as demonstrated by Fig. 6). Using least square fitting with $N = M$ the condition number of the **E** matrix is 24 in Fig. 3. The conditioning of the **E** matrix can be rapidly improved by increasing the M/N ratio and by increasing the readout gradient strength in proportion to keep the same spatial resolution. For example, for $M = 1024$, $N = 512$, $G_{readout} = -2 \times G_{encoding}$ (the spatially encoded time domain image is centered in SW by extending the encoding gradient by $T_p/2$ after the frequency sweep pulse) the condition number of the **E** matrix become ~1.3, very close to that of the unitary Fourier matrix (1.0), therefore, minimizing noise amplification in the reconstructed images. In the special case of linear frequency sweep using chirp pulse or modified chirp pulses, the *k* space echo

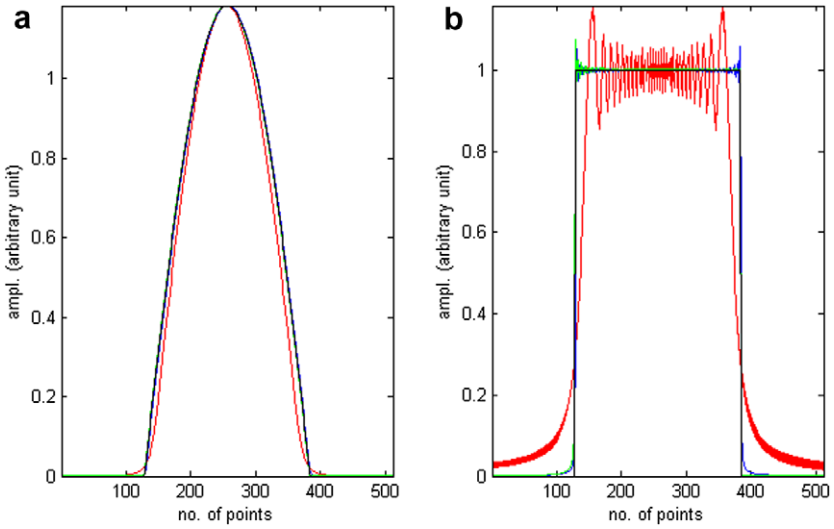

Fig. 6. Spatial encoding and image reconstruction for the nonlinear frequency sweep are described in the text. (a) spatially encoded time domain image (red), its Fourier transform (blue), and least square fitted image (green) of the same one-dimensional half sine-shaped ($\sin(x)$, $x \sim [0, \pi]$) spin density distribution (black) as in Fig. 3(a). (b) Spatially encoded time domain image (red), its Fourier transform (blue), and least square fitted image (green) of the same one-dimensional rectangle ($\Pi(x)$) spin density distribution (black) as in Fig. 3(b). Parameters for gradients, the modified chirp pulse and data acquisition used in simulation were identical to those in Fig. 3 except for the nonlinear frequency sweep.

$F(k(t))$ shows an interesting resemblance to $\rho(x_k)$, much unlike conventional imaging with RF-free phase encoding in which the k space echo bears no resemblance to $\rho(x)$ at all. As shown by Eqs. (10) and (11) the $\rho(x)$ can be accurately retrieved using Fourier transform. We note that the analytical form of Eq. (10) states that the spatially encoded time domain image is the Fourier transform of the relaxation-weighted spin density $\rho(x)$ multiplied by a high order phase term.

The effects of truncating k-space data by the finite sampling window are extensively documented in the MRI literature. In conventional gradient echo imaging, spin packets with large susceptibility gradient along the phase encoding and readout directions form gradient echoes outside of the sampling widow when echo shift $\geqslant$ SW/2 in either direction, leading to complete signal loss. With linear frequency sweep encoding, spin packets form echoes sequentially across the sampling window. For off-centered spin packets the effect of echo shift depends on the relative polarity of the background gradient. For example, for spin packets forming an echo at SW/4, a shift along the negative frequency direction by SW/4 would cause complete signal loss in gradient echo image while the same spin packet need to be shifted by 3SW/4 in the positive frequency direction to generate the same signal loss. While previous in vivo applications of frequency sweep encoding have been limited to low resolution (along the direction of frequency sweep encoding) spin–echo imaging, the in vivo results shown in Figs. 4 and 5 demonstrate that this method may become a viable competitor for high resolution and high fidelity imaging.

In conclusion, combining Fourier transform and frequency sweep encoding allows formation of high fidelity images comparable to conventional high resolution images. The unique FIFO and LIFO features of sequential excitation and encoding with continuous frequency sweep may prove to be a fruitful venue for developing novel imaging methods.

Acknowledgment

This work is supported by the Intramural Research Program of the NIH, NIMH.

References

[1] D.B. Twieg, The k-trajectory formulation of the NMR imaging process with applications in analysis and synthesis of imaging methods, Med. Phys. 10 (1983) 610–621.
[2] S. Ljunggeren, A simple graphical representation of Fourier-based imaging methods, J. Magn. Reson. 54 (1983) 338.
[3] P. Mansfield, A.A. Maudsley, T. Baines, Fast scan proton density imaging by NMR, J. Phys. E Sci. Instrum. 9 (1976) 271.
[4] J.B. Ra, C.Y. Rim, Fast imaging using subencoding data sets from multiple detectors, Magn. Reson. Med. 30 (1993) 142–145.
[5] I.J. Lowe, R.E. Wysong, DANTE ultrafast imaging sequence (DUFIS), J. Magn. Reson. B 101 (1993) 106–109.
[6] Z.H. Cho, Y.M. Ro, A DANTE fast MR imaging using frequency modulation, in: Proceedings, SMR, 3rd Annual Meeting, 1995, p. 496.
[7] H. Nilgens, M. Thelen, J. Paff, P. Blümler, B. Blümich, Hadamard NMR imaging with slice selection, Magn. Reson. Imaging 14 (1996) 857–861.
[8] M.E. Meyerand, E.C. Wong, A time encoding method for single-shot imaging, Magn. Reson. Med. 34 (1995) 618–622.
[9] S.M. Wright, M.P. McDougall, Single echo acquisition MRI using RF encoding, NMR Biomed. 22 (2009) 982–993.
[10] G.A. Morris, R. Freeman, Selective excitation in Fourier transform nuclear magnetic resonance, J. Magn. Reson. 29 (1978) 433.
[11] J.G. Pipe, Spatial encoding and reconstruction in MRI with quadratic phase profiles, Magn. Reson. Med. 33 (1995) 24–33.
[12] L. Frydman, T. Scherf, A. Lupulescu, The acquisition of multidimensional NMR spectra within a single scan, Proc. Natl. Acad. Sci. USA 99 (2002) 5858–5862.
[13] Y. Shrot, L. Frydman, Spatially encoded NMR and the acquisition of 2D magnetic resonance images within a single scan, J. Magn. Reson. 172 (2005) 179–190.
[14] A. Tal, L. Frydman, Spatial encoding and the single-scan acquisition of high definition MR images in inhomogeneous fields, J. Magn. Reson. 182 (2006) 179–194.
[15] R. Chamberlain, J.Y. Park, C. Corum, E. Yacoub, K. Ugurbil, C.R. Jack Jr., M. Garwood, RASER: a new ultrafast magnetic resonance imaging method, Magn. Reson. Med. 58 (2007) 794–799.
[16] N. Ben-Eliezer, Y. Shrot, L. Frydman, High-definition, single-scan 2D MRI in inhomogeneous fields using spatial encoding methods, Magn. Reson. Imaging (14) (2009) (Epub ahead of print).
[17] R. Paquin, P. Pelupessy, G. Bodenhausen, Cross-encoded magnetic resonance imaging in inhomogeneous fields, J. Magn. Reson. 201 (2009) 199–204.
[18] S. Li, J. Shen, Integrated RF probe for in vivo multinuclear spectroscopy and functional imaging of rat brain using an 11.7 Tesla 89 mm bore vertical microimager, MAGMA 18 (2005) 119–127.
[19] Z. Chen, S.S. Li, J. Yang, D. Letizia, J. Shen, Measurement and automatic correction of high-order B0 inhomogeneity in the rat brain at 11.7 Tesla, Magn. Reson. Imaging 22 (2004) 835–842.
[20] J. Mao, T.H. Mareci, Andrew ER Experimental study of optimal selective 180 radiofrequency pulses, J. Magn. Reson. 79 (1988) 1–10.

[21] S. Conolly, G. Glover, D. Nishimura, A. Macovski, A reduced power selective adiabatic spin–echo pulse sequence, Magn. Reson. Med. 18 (1991) 28–38.
[22] D.C. Noll, D.G. Nishimura, A. Macovski, Homodyne detection in magnetic resonance imaging, IEEE Trans. Med. Imaging 10 (1991) 154–163.
[23] J.H. Duyn, P. van Gelderen, T.Q. Li, J.A. de Zwart, A.P. Koretsky, M. Fukunaga, High-field MRI of brain cortical substructure based on signal phase, Proc. Natl. Acad. Sci. USA 104 (2007) 11796–11801.
[24] J. Frahm, A. Haase, D. Matthaei, Rapid three-dimensional MR imaging using the FLASH technique, J. Comput. Assist. Tomogr. 10 (1986) 363–368.